Diagnosis of Convective and Mesoscale Motions During Phase III of GATE

RICHARD H. JOHNSON

Department of Atmospheric Science, Colorado State University, Fort Collins 80523

(Manuscript received 6 April 1979, in final form 7 November 1979)

ABSTRACT

Observational evidence from GATE suggests that a significant fraction of precipitation in tropical disturbances over the eastern Atlantic occurs beneath anvil-type mesoscale convective systems that are frequently associated with intense cumulonimbus convection. A diagnostic model is developed that includes heat, moisture and mass transports by both the convective-scale and mesoscale components of these systems. An entraining plume model is used for individual convective-scale elements yielding a spectral distribution of cumulus sizes. Mesoscale downdrafts are modeled using a bulk cloud model. A parameterization links properties of the mesoscale systems to those of associated deep convective-scale (cumulonimbus) clouds. A method based on a subjective comparison of model results to observed cloud cover is used to determine mesoscale downdraft areas in relation to cumulonimbus areas. For this reason only qualitative results derived from application of the theory can be considered reliable.

The model is applied to GATE tropical-wave composite data (Thompson *et al.*, 1979) for Phase III. Radiative heating rates derived from observations during this period and storage of water in clouds determined from satellite and ground-based whole-sky camera cloud coverage data are included in the study. Diagnostic model results may be interpreted as indicating the existence of deep convection and mesoscale downdraft systems well in advance of the composite wave trough, followed by suppressed low-level cloud activity with a later increase in deep cumulus convective and mesoscale downdrafts to a maximum centered at the trough axis. Multiple layers of cumulus cloud detrainment are diagnosed to occur in the vicinity of the wave trough. Convective-scale and mesoscale downdrafts are diagnosed to be important contributors to the mass, heat and water budgets of the composite wave, indicating that their effects should be included in cumulus parameterization schemes.

1. Introduction

Observations from the GARP Atlantic Tropical Experiment (GATE) have shown, at least in the eastern Atlantic, that a complex mix of convective disturbance types exists in the equatorial trough region during summer months. However, recent evidence has indicated that there are certain basic precipitation structures common to many deep convective systems or cloud clusters that exist in this region. In a radar study of a tropical cloud cluster that passed over the ship array during Phase III of GATE, Leary and Houze (1979a) have identified both convective-scale (~1–10 km) and mesoscale (~100 km) precipitation features as primary components of the cluster. The two scales of convection commonly coexist within mesoscale convective disturbances having lifetimes of ~12–24 h. In their mature stages the mesoscale precipitation features possess a region of convective cells along their leading edge and a large area of horizontally uniform precipitation to the rear. The mesoscale rain areas have been found to account for a significant fraction of the total precipitation in GATE. López (1978) contends that the majority of precipitation in Phase III was from mesoscale convective systems. Recently, Cheng and Houze (1979) have determined using radar data that 43% of the total precipitation in GATE fell in the uniform mesoscale rainfall regions of these convective systems.

The mesoscale precipitation features generally characteristic of cloud clusters are similar, though less intense, to those observed in tropical squall lines (Leary and Houze, 1979a). GATE squall lines having convective-scale updrafts with nearly saturated convective-scale downdrafts and associated unsaturated mesoscale downdrafts have been reported on by Houze (1977) and Zipser (1977). Similar squall line systems that exist over Venezuela have been described in a study by Miller and Betts (1977). While strong squall lines were relatively rare during GATE (four in Phase III), cumulonimbus convection with associated mesoscale precipitation areas was rather common. The mesoscale downdrafts, felt to be common features of both the squall and non-squall clusters (Leary and Houze, 1979a), are thought to be sustained primarily by evaporation of precipitation beneath widespread anvil clouds

0022-4928/80/040733-21$09.25

that themselves may be maintained for rather long periods of time by mesoscale upward motion (Leary and Houze, 1979b). Brown (1979) has developed a numerical model that simulates a number of the observed features of these types of mesoscale downdrafts.

Efforts aimed at determining the properties of cumulus populations through diagnostic models (Yanai *et al.*, 1973; Ogura and Cho, 1973; Nitta, 1975, 1977; Johnson, 1976) have treated only the effects of convective-scale transports on the large-scale flow. The evidence cited above suggests, however, that mesoscale precipitation systems may contribute importantly to the total large-scale convective mass, heat and moisture transports. In this paper the attempt is made to include the effects of both convective-scale and mesoscale transports in a diagnostic model to determine properties of cumulus populations in tropical wave disturbances. The mesoscale component of the proposed model is based to a large extent on GATE observations of mesoscale downdraft systems.

We adopt the working hypothesis that although convective systems take many forms, their net effect on the mass and energy budgets of the synoptic scale can be reasonably approximated as if they consisted of convective-scale updrafts and downdrafts modeled as saturated, entraining plumes and an unsaturated mesoscale downdraft having properties derived from a simple bulk cloud model. The area coverage of the mesoscale downdrafts is directly related to that of deep cumulonimbus convection. This model contrasts with that developed by Nitta (1977) which uses a bulk cloud model for all precipitation downdrafts.

The model is applied to the tropical wave composite data of Thompson *et al.* (1979) for Phase III of GATE. Effects of storage of cloud water on the GATE B-scale are considered. Radiative heating rates reported by Cox and Griffith (1979) for Phase III are incorporated into this study.

It will be seen that a precise determination of the relative magnitudes of mesoscale and convective-scale downdrafts is not possible due to limited information from GATE concerning areal coverages by these downdraft systems. However, a realistic estimate of the appropriate values will be given based on physical interpretation of model results.

A finding of this study, namely, that mesoscale convection contributes importantly to the mass and energy budgets of tropical disturbances, has been independently determined by Leary and Houze (1980). Their results are based on a diagnostic model developed by Houze *et al.* (1980) that includes effects of both convective-scale and mesoscale updrafts and downdrafts. Results of sensitivity tests for their model are reported by Cheng and Houze (1980).

2. Large-scale budget equations

Within the large scale, on the order of the GATE B-scale ship array ($\sim 10^5$ km^2), both cumulus ($\sim 1-10$ km) and mesoscale (~ 100 km) convective systems are considered. These systems may typically comprise ~ 1 and $\sim 10\%$, respectively, of the total area. The region between the two types of active-cloud systems will be called the active-cloud environment.

It will not be assumed that the active-cloud environment is cloud free. On the contrary, in accordance with the numerous GATE observations of total cloudiness (e.g., Holle *et al.*, 1979), it is assumed that the active-cloud environment may be occupied by a certain amount (to be determined) of inactive clouds, i.e., nonprecipitating, mostly stratiform-type clouds, containing negligible vertical motion. Obviously, meteorological variables, especially specific humidity, are therefore not horizontally uniform in the active-cloud environment. However, for simplicity, a single value of each variable will be ascribed to the active-cloud environment at each level. Since the active-cloud environment covers most of the total area, we assume that values in this region (designated by a tilde in later sections) are those provided by composited radiosonde data (Section 3).

Averaging the water vapor and heat equations over the large-scale area considered here, designating this average by an overbar, we obtain

$$-\frac{Q_2}{L} \equiv \frac{\partial \bar{q}}{\partial t} + \nabla\cdot\bar{\mathbf{v}}\bar{q} + \frac{\partial}{\partial p}\bar{\omega}\bar{q} - \bar{S}_q$$

$$= -\frac{\partial}{\partial p}(\overline{q'\omega'}) + \bar{e} - \bar{c}, \qquad (1)$$

$$Q_1 \equiv \frac{\partial \bar{s}}{\partial t} + \nabla\cdot\bar{\mathbf{v}}\bar{s} + \frac{\partial}{\partial p}\bar{\omega}\bar{s} + L\bar{S}_q$$

$$= -\frac{\partial}{\partial p}(\overline{s'\omega'}) + L(\bar{c} - \bar{e}) + Q_R, \qquad (2)$$

where q is the specific humidity or water vapor mixing ratio, $s \equiv c_pT + gz$ the dry static energy, c_p specific heat for dry air, T temperature, g acceleration of gravity, z geopotential height, ω the vertical pressure velocity, Q_1 the "apparent heat source" (after Yanai *et al.*, 1973), Q_2 the "apparent moisture sink", Q_R the net radiative heating rate and L the latent heat of vaporization or fusion. $\bar{e}$ is the evaporation rate of cloud condensate in the large-scale area due to clouds that are produced within that area during a characteristic time interval for the large scale. Similarly, $\bar{c}$ is the condensation rate for condensate that remains in the area during this time interval. Additional evaporation or condensation may occur in the large-scale area associated

CATEGORY	HOUR (GMT) 00	03	06	09	12	15	18	21	TOTAL OBSERVATIONS
1	0	0	1	3	3	5	4	0	16
2	6	4	2	1	1	1	2	6	23
3	1	2	4	4	3	2	0	0	16
4	3	2	2	2	2	3	4	3	21
5	2	3	2	2	2	1	2	3	17
6	3	3	4	4	5	3	2	2	26
7	2	2	1	2	2	4	4	2	19
8	3	4	4	2	2	1	2	4	22

FIG. 1. Frequency distribution of composite wave observations (160 total). Diagonal lines indicate average time of passage of each category.

with a transport of cloud or precipitation into or out of the region. This external water vapor source is represented by $\bar{S}_q$ and is included in the definition of Q_2 and Q_1 as large-scale source terms. $\bar{S}_q$ will be referred to as a cloud-storage term. The method used to determine its value is described in Section 4.

3. Composite wave data

The model developed in this study will be used to determine convective transports and cloud population properties within the B-scale area of GATE using data reported on by Thompson *et al.* (1979). These authors have prepared heat and moisture budgets from the surface to 100 mb at 3 h intervals for Phase III with the use of wind, temperature and moisture fields obtained from A/B and B-scale ship rawinsonde data fitted quadratically over space and linearly over 12 h time intervals by the method of least squares. In addition, the 3 h data are composited according to the phase of African waves (Reed *et al.*, 1977) to give average budgets in various parts of the wave disturbance. In the following discussions these data will be referred to eight categories of the composite wave, category 4 being the trough, 8 the ridge, 2 the position of maximum northerly wind at 700 mb and 6 the position of maximum southerly wind at 700 mb. Categories 1, 3, 5 and 7 occupy intermediate positions. Basic fields of horizontal wind **v**, temperature T, specific humidity q, vertical p velocity ω, and Q_1 and Q_2 at 3 h intervals for Phase III were provided from the work of Thompson *et al.* (1979). Additional data obtained from these authors include surface evaporation measurements (based on the bulk-aerodynamic method using data from four B-scale ships) and precipitation measurements (based on radar observations) at 6 h intervals. The reader is referred to their work for descriptions of the above variables and further details pertaining to the characteristics of this data set.

The wave composite is based on the passage of six wave disturbances across the A/B and B-scale network of ships during the 20-day period of Phase III. Since observations were at 3 h intervals, a total of 160 fitted soundings are used in the analysis. Fig. 1 gives the frequency of occurrence of each category. It is apparent that the times of passage of most wave categories over the center of the B array are not randomly distributed. Diagonal lines in the figure indicate the average time of passage of each category. Note, for example, that the wave trough (category 4) passage occurs most frequently in the late afternoon, near 1800 GMT (1630 LST). Thompson *et al.* (1979) show that maximum precipitation is associated with the wave trough. The fact that African waves traversed the ship array in such a way that peak rainfall amounts occurred in early afternoon has been discussed by McGarry and Reed (1978). Although there are an average of 20 observations for each category, note that in some cases large differences in the totals exist from one category to the next.

The apparent heat source Q_1 (Fig. 2) has a maximum at 600 mb in category 4 of 10°C day^{-1}. The apparent moisture sink Q_2 has a pronounced maximum ~11°C day^{-1} near 900 mb in category 3 (Fig. 3). The peaks in Q_1 and Q_2 are larger and centered about one or two categories farther east (to the right) than the peaks found by Johnson (1978) using African wave data from the same latitudinal band

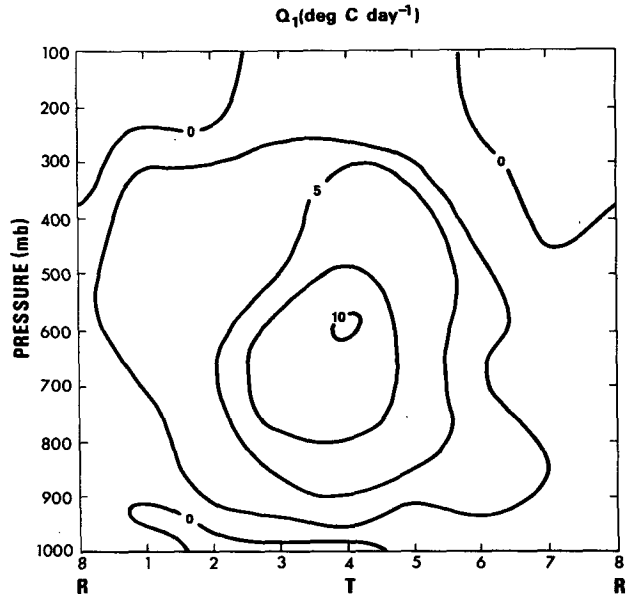

FIG. 2. Apparent heat source Q_1 including cloud-water storage.

based on the study of Reed *et al.* (1977). The difference in the two results can be attributed to 1) the fact that the Reed *et al.* (1977) composite wave represents a combination of data taken over land and ocean whereas this study uses strictly data over the ocean and 2) the Reed *et al.* (1977) compositing was on the basis of 700 mb flow criteria at a latitude band 4° to the north of the center of the B-scale array. It is expected that the data from Thompson *et al.* provide a more accurate representation of the structure of African waves over the ship array.

4. Cloud-water storage

Although the budgets considered in this study are for a large-scale area, the abundant cloudiness observed during GATE dictates a consideration of the effects of variable cloud amount. Based on a determination of B-scale cloudiness from ground-based whole-sky camera photographs, Holle *et al.* (1979) found that on the average 79% of the sky was obscured by clouds during Phase III. Their data plus the cloud cover data given by Thompson *et al.* (1979) will be used in this study to evaluate the cloud-storage terms in (1) and (2).

The horizontally averaged cloud-condensate mixing ratio is

$$\bar{q}_c = \sigma_{ac} q_{cac} + \sigma_{ic} q_{cic}, \tag{3}$$

where σ_{ac} and σ_{ic} are the fractional areas occupied by active and inactive clouds, respectively. Active clouds are defined as those containing strong vertical motions, i.e., convective-scale clouds, and inactive clouds are those having negligible or weak vertical motion. Since convective-scale clouds occupy ~1% of the total area whereas inactive clouds may occupy 10–50% of the area or more, and, further, the total condensate mixing ratios for active and inactive clouds (q_{cac} and q_{cic}) likely differ on the average by no more than a factor of ~5, then to a fair approximation

$$\bar{q}_c \approx \sigma_{ic} q_{cic}. \tag{4}$$

The total change of $\bar{q}_c$ in a coordinate system moving at speed $c(-8 \text{ m s}^{-1})$, the phase speed of the westward propagating waves, is $-\bar{S}_q$ (x increasing to east), i.e.,

$$\frac{d\bar{q}_c}{dt} = (\bar{u} - c) q_{cic} \frac{\partial \sigma_{ic}}{\partial x} = -\bar{S}_q, \tag{5}$$

where we have assumed a constant zonal velocity $\bar{u}$, have neglected meridional and vertical advection, and have assumed that q_{cic} is roughly uniform across the wave.

Two sources of data are combined to determine σ_{ic} for the composite wave. Cloudiness data derived from whole-sky photographs at hourly intervals

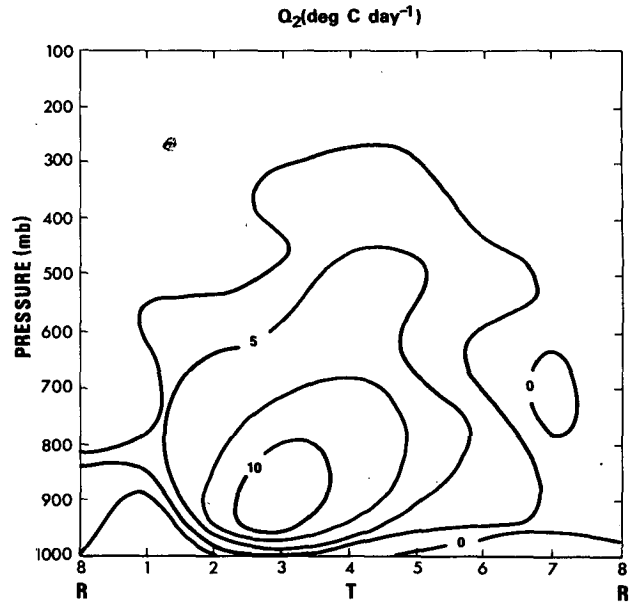

FIG. 3. Apparent moisture sink Q_2 including cloud-water storage.

from 0800 to 1900 LST (0930–2030 GMT) from the ships *Dallas, Gilliss, Oceanographer* and *Researcher* have been provided by R. Holle (NHEML, Coral Gables) and J. Simpson (University of Virginia). These ground-based measurements of sky cover, while generally providing good estimates of low cloud cover, give less reliable estimates of middle and high cloud amount due to frequent obscuration by lower clouds. Since satellite measurements likely provide a better determination of high cloud amount, especially in disturbed situations, the satellite-derived middle and high cloud coverages of Thompson *et al.* (1979) are blended with the ground-based photographic measurements to obtain an optimum determination of the full tropospheric cloud coverage.

The Phase III cloudiness data of Holle *et al.* were averaged over 3 h intervals at 0900, 1200, 1500 and 1800 GMT for each ship, then a four-ship average was formed and the data were composited into the eight wave categories. Three cloud groups were observed: low clouds (base below 2 km), middle clouds (base between 2 and 8 km) and high clouds (base above 6 km). Note from these definitions that low clouds do not necessarily imply shallow clouds. Some clouds in this category may well extend through the entire troposphere. This complication makes a precise determination of cloud volumes very difficult. Cloud-coverage values were also made for a number of middle- or high-level clouds for which bases could not be determined. The observations in this group have been divided equally between the middle and high cloud classifications.

In order to combine the two sources of information, an overlap factor for middle and high clouds

TABLE 1. Percent cloud coverage for three cloud classifications.

Cloud type	Category 1	2	3	4	5	6	7	8
High	25	67	65	71	67	24	20	17
Middle	30	67	65	71	67	52	34	40
Low	18	64	50	44	32	36	28	22
Number of low cloud cases	15	5	9	11	7	14	12	7

was determined. Since low-cloud cover in the wave-ridge region (categories 1, 6, 7, 8) was generally less than 30% as observed by the whole-sky cameras, ground-based estimates of middle- and high-cloud amount in this region were considered reliable. Effects of obscuration of high clouds by middle clouds are probably minimal here since sequences of pictures are used in the analysis. The sums of the middle- and high-cloud amount in these categories were then compared to the middle- plus high-cloud coverage data given by Thompson *et al.* (1979) based on infrared satellite images. Ratios of the two sums give estimates of the degree to which high and middle clouds overlap in space. Using the average overlap factor thus determined for the ridge, the middle-plus high-cloud amount values for categories 2–5 given by Thompson *et al.* were adjusted to give total middle- and high-cloud amounts (including overlap). Next this total amount was arbitrarily divided equally between middle and high clouds. The resulting cloud coverages are given in Table 1.

The percentages given in Table 1 must be interpreted carefully. First, in several categories the number of available cloudiness observations is small compared to the total possible (an average of 20, see Fig. 1). Second, the percentage indicated for a particular cloud type does not imply that the entire volume represented by that cloud stratum is filled with that percentage of cloud. Some assumption must be made regarding the latter point. We assume arbitrarily as a rough upper limit that both middle and high clouds occupy one-half the depth of their respective layers (2–6 km for middle clouds and 6 km to the tropopause for high clouds). Percent coverage for low clouds is assumed to vary linearly from the value given in the table at cloud base to the middle-cloud value, determined by the method above, at 2 km. At best, we expect the above determination of cloud volumes for the composite wave to be of semi-quantitative value, at least reliable enough to provide upper-bound estimates of the cloud storage effects.

Table 1 indicates that the greatest low-cloud cover occurs at and in advance of the wave trough. The value in category 2 is considered less reliable because of the limited number of observations. Greater than 50% middle-cloud cover occurs from category 2–6. High clouds are most abundant in categories 2–5.

Using observations of $\bar{u}$ and an assumed q_{cic} profile that gives a decrease from ~1.0 g kg^{-1} at cloud base to ~0.5 g kg^{-1} near the tropopause, $d\bar{q}_c/dt$ was computed from (5). The results shown in Fig. 4 indicate that this term can be as large as ~20% of Q_2 (in a vertically integrated sense) in categories 1, 5 and 6. These are the regions of the wave where cloud amount changes most rapidly (Fig. 18, Thompson *et al.*, 1979) and, therefore, cloud storage effects would be expected to be greatest. The contribution in other regions is small. It is expected, and later verified, that cloud-water storage is of some importance in the water-vapor budget for categories where cloud amount is rapidly changing (see also McNab and Betts, 1978). Until more accurate measurements of total cloudiness and cloud water contents are available, however, the above results regarding cloud storage effects cannot be considered conclusive.

5. Radiative heating rates

Previous diagnostic studies of this nature have used climatological values of net radiative heating rates (e.g., those of Dopplick, 1972) in determining convective transports. For this study radiative divergence estimates at 6 h intervals for Phase III of GATE prepared by Cox and Griffith (1979)

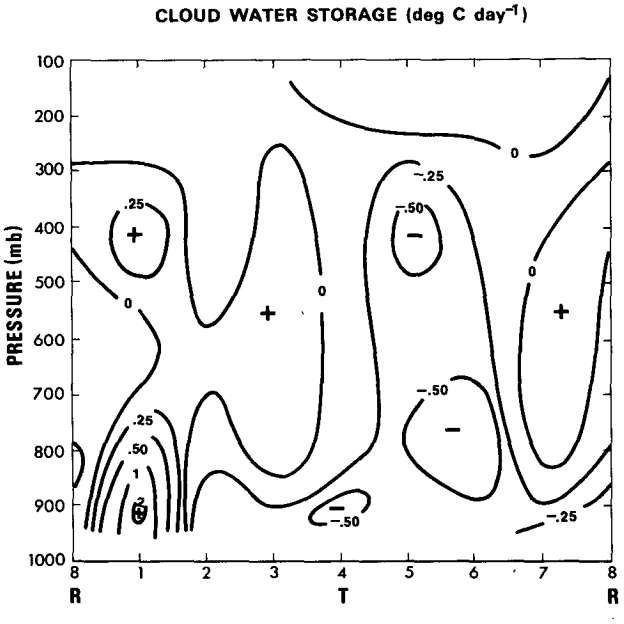

FIG. 4. Cloud-water storage $-L\bar{S}_q$ determined from whole-sky camera data (Holle *et al.*, 1979) and satellite data (Thompson *et al.*, 1979). Values indicated are felt to provide an upper-bound estimate of storage effects.

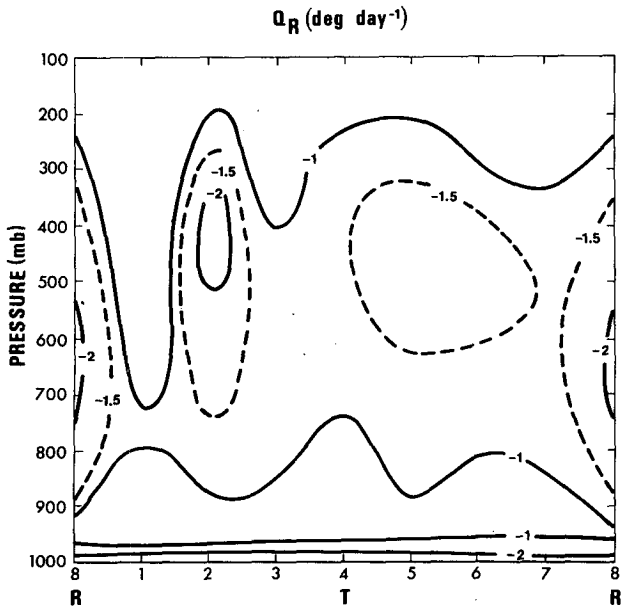

FIG. 5. Net radiative heating rates for composite wave.

have been obtained. These values have been determined from composites of longwave and shortwave radiative divergence profiles derived from radiative transfer computational routines applied to GATE rawinsonde data. Geostationary satellite data have been used to form the composites. Adjustments in the computed values have been made to achieve consistency with radiation data collected during GATE.

Radiative heating rates for the composite wave are shown in Fig. 5. There exist significant differences in the values between several of the categories. Note, for example, that there is a pronounced minimum in the cooling rates in category 1. The explanation for this feature is apparent if one considers that all but one observation in this category occurred between 0900 and 1800 GMT (1030 and 1930 LST, a period of maximum shortwave heating (Fig. 1). Most category 2 and 8 observations, on the other hand, occurred at night. As a result relatively strong cooling is present in these categories. In general, the nonrandom frequency distribution of wave categories exerts a greater control on the net radiative heating distribution than the variable cloud amount across the wave on this synoptic scale. The extensive middle and upper tropospheric cloudiness in the wave-trough region contributes to the cooling maximum in the 400–600 mb layer, the same interval within which the values given by Dopplick (1972) show a relative minimum. The data of Cox and Griffith show a relative cooling minimum near 950 mb in contrast to Dopplick's results which exhibit a monotonic increase in the cooling rate from ~ -1.0 to ~ -1.8°C day^{-1} from 700 to 1000 mb. Explanations for these differences are given by Cox and Griffith.

The total tropospheric radiative divergence (the integral of Q_R through the depth of the troposphere) is shown in Table 2. Note the significant differences in categories 1, 2 and 8 from the mean of -120 W m^{-2}. This result along with the observation that the radiative term is nearly always larger than the term

$$g^{-1}\int_{p_T}^{p_s}(Q_1 - Q_2)dp$$

in the expression for the vertical eddy heat flux at the earth's surface F_0, where

$$F_0 = F(p_s) \equiv g^{-1}\int_{p_T}^{p_s}(Q_1 - Q_2 - Q_R)dp, \quad (6)$$

TABLE 2. Vertically integrated Q_R, $Q_1 - Q_2$ and $Q_1 - Q_2 - Q_R$ for the composite wave and observed $S_0 + LE_0$. Units: W m^{-2}. Also observed precipitation P_{OBS} and computed precipitation, with and without cloud water storage effects, P_0 (CWS) and P_0 (NO CWS). Units: mm day^{-1}.

	Category								
	1	2	3	4	5	6	7	8	Mean
$g^{-1}\int_{p_T}^{p_s} Q_R dp$	−59	−160	−98	−113	−137	−119	−111	−163	−120
$g^{-1}\int_{p_T}^{p_s}(Q_1 - Q_2)\,dp$	69	−87	−47	49	48	30	−10	−59	−1
F_0	128	73	51	162	185	149	101	104	119
$S_0 + LE_0$	84	100	129	134	142	128	129	100	118
P_{OBS}	3.6	16.2	19.5	22.0	21.1	5.9	7.9	4.0	12.5
P_0 (CWS)	7.5	15.8	23.3	23.7	17.6	11.9	6.3	7.5	14.2
P_0 (NO CWS)	8.7	15.4	23.3	23.1	16.5	10.8	6.4	7.2	13.9

where p_s is the surface pressure and p_T the tropopause pressure, leads one to conclude that the use of constant Dopplick profiles for the wave could lead to significant errors in diagnosed convective fluxes, especially in the lower troposphere (see Yanai *et al.*, 1976). In theory (Yanai *et al.*, 1973) the value of F_0 should agree with the sum of the observed sensible and latent heat fluxes $S_0 + LE_0$. While the mean values for the wave agree rather well (Table 2), it is apparent that rather large disagreements exist in several of the categories. Nitta (1977) also finds disagreement between computed and observed vertical eddy heat fluxes for different convective situations using GATE data. The causes of this discrepancy are difficult to separately identify. Most likely, errors in Q_1, Q_2 and Q_R, and to a lesser extent errors in S_0 and E_0, are contributing to the differences in these independent estimates of F_0.

The observed precipitation is also presented in Table 2 and indicates that the heaviest rainfall occurs in categories 2–5. Precipitation rates computed from the water-vapor budget with and without cloud storage effects included are compared [from Eq. (26), Section 7]. The computed rate in category 1 is reduced by ~20% when storage effects are considered, whereas in 5 and 6 rates are increased by ~10%. Elsewhere the results do not change significantly.

6. Diagnostic model

In this analysis the individual contributions to convective processes by convective-scale updrafts, downdrafts (hereafter designated by subscripts u, d) and mesoscale updrafts and downdrafts (subscripts mu, md) will be considered. The evaporation rate e is given by

$$e = e_u + e_d + e_{mu} + e_{md}, \tag{7}$$

where e_u and e_{mu} represent evaporation of detrained hydrometers from convective-scale and mesoscale updrafts, respectively. It will be assumed that the only detrainment from downdrafts takes place below the level of cloud base updrafts so that e_d and e_{md} represent evaporation within convective-scale and mesoscale downdrafts, respectively. In accordance with the observations of Zipser (1977), air within convective-scale downdrafts is assumed to be close to saturation, whereas within mesoscale downdrafts air is unsaturated (to be discussed further later). The condensation rate c is

$$c = c_u + c_{mu} \tag{8}$$

since no condensation occurs in downdrafts.

Following the previous work of Johnson (1976), convective-scale updrafts and downdrafts are represented as entraining plumes (with a "top-hat" profile assumed for variables within these plumes) having a spectrum of sizes given by their entrainment rates λ (inversely proportional to cloud radius):

$$\frac{1}{m_u(\lambda,p)}\frac{\partial}{\partial p} m_u(\lambda,p) = -\frac{\lambda H}{p}, \tag{9}$$

$$\frac{1}{m_d(\lambda,p)}\frac{\partial}{\partial p} m_d(\lambda,p) = \frac{\lambda H}{p}, \tag{10}$$

and $m_u(\lambda,p)$ and $m_d(\lambda,p)$ are the mass fluxes within individual updrafts and downdrafts per unit λ. Values of m have units of mass flux per unit area when divided by g. Here $H \equiv R_d T_v/g$ is the scale height of an atmosphere with a virtual temperature $T_v \approx T(1 + 0.61q)$ and R_d is the gas constant for dry air. Both drafts are assumed to entrain the same air from the active-cloud environment. The thermodynamic properties of cumulus-scale updrafts and downdrafts are determined from

$$m_u(\lambda,p)\frac{\partial h_u(\lambda,p)}{\partial p} = \frac{\partial m_u(\lambda,p)}{\partial p}[\bar{h}(p) - h_u(\lambda,p)], \tag{11}$$

$$m_d(\lambda,p)\frac{\partial h_d(\lambda,p)}{\partial p} = \frac{\partial m_d(\lambda,p)}{\partial p}[\bar{h}(p) - h_d(\lambda,p)], \tag{12}$$

where $h \equiv s + Lq$ is the moist static energy.

Cloud-base level p_B for each updraft used to solve (11) is taken as the lifting condensation level of the surface air: 950, 960, 965, 965, 965, 960, 955, 955 mb for categories 1–8, respectively, of the Thompson *et al.* (1979) composite wave. It is evident that cloud base is suppressed in the wave-trough region where convective activity is a maximum (see, e.g., Brümmer, 1978). As in Johnson (1976), the updraft air at cloud-base level is assumed saturated with virtual temperature identical to that of the environment. Cumulus updrafts are assumed to detrain at the level where cloud buoyancy (including cloud condensate effects) vanishes. In reality cumulonimbus clouds frequently overshoot the zero-buoyancy level by as much as 1 or 2 km. Some consideration has been given to this effect and it has been determined that inclusion of overshooting primarily has the effect of raising the maximum detrainment level in the upper troposphere by 1 or 2 km. Rather than attempting to model the uncertain behavior of overshooting, we will simply keep this qualitative effect in mind when interpreting later results.

Cumulus downdrafts originate in the model at a level above p_B given by three-fourths the pressure depth of the adjacent updrafts. Properties of air at

the downdraft originating level are assumed in Johnson (1976) to be different from those of the surrounding environmental air. John M. Brown has pointed out that with this assumption, the integral equation (25) in that paper, as well as several preceeding equations, is missing a term containing the product of the downdraft mass flux and the difference between cloud and environment moist static energy at the originating level. Physically, such a term arises when it is assumed that air enters downdrafts having properties different from those of the environment, for then the removal of this air from the environment changes the average properties of the environment. A reanalysis of results in Johnson (1976), however, reveals that this term is present only in the mid- to lower troposphere and on the average in this layer is less than 2% of the largest terms in the equation. Therefore, with justification, the assumption used in Johnson (1976) that the moist static energy at the downdraft originating level is equal to the saturation moist static energy of the environment is repeated in this study without including the additional term described above. The convective-scale downdraft mass flux is expressed in terms of the updraft mass flux using a parameter $\epsilon(\lambda)$ where

$$\epsilon(\lambda) \equiv \frac{m_0(\lambda)}{m_B(\lambda)} .$$

In this expression the downdraft-originating-level-mass-flux distribution function $m_0(\lambda)$ and the cloud-base-mass-flux distribution function $m_B(\lambda)$ are given by the solutions of (9) and (10):

$$m_u(\lambda,p) = m_B(\lambda)\eta_u(\lambda,p), \tag{13}$$

$$m_d(\lambda,p) = m_0(\lambda)\eta_d(\lambda,p), \tag{14}$$

where

$$\eta_u(\lambda,p) = \exp\left\{\int_p^{p_B} \frac{\lambda H}{p}\, dp\right\} ,$$

$$\eta_d(\lambda,p) = \exp\left\{\int_{p_0}^{p} \frac{\lambda H}{p}\, dp\right\} .$$

In the above p_B is cloud base and p_0 the convective-scale downdraft originating level. Although in previous work $\epsilon(\lambda)$ has been specified as a constant for all cloud types, this approximation is not necessary. A determination of the precise functional form for $\epsilon(\lambda)$ from observations is difficult. In this study we make the assumption that ϵ is larger for deep, precipitating clouds than for shallow, nonprecipitating clouds, i.e.,

$$\epsilon(\lambda) = \epsilon(\lambda = 0)\left(1 - \frac{\lambda}{\lambda_{\max}}\right) , \tag{15}$$

where $\epsilon(\lambda = 0)$ is ϵ for the deepest clouds and $\lambda_{\max}$ is the entrainment rate for the shallowest clouds. In the study of Johnson (1978) it was found that in different regions of a composite wave for Phase III of GATE there were significant differences in the optimum value of ϵ as determined using observed precipitation. This result suggests that the intensity of downdrafts from deep clouds may be controlled to some extent by large-scale processes, e.g., vertical wind shear, convergence-divergence patterns, relative humidity or others. While it is realistic to expect ϵ for deep clouds to vary from convectively undisturbed to disturbed conditions, such a variation for shallow clouds would seem unrealistic. The assumption given by (15) eliminates confusion over this matter since $\epsilon \approx 0$ for the shallowest clouds regardless of the value of ϵ for the deep clouds.

In this study a simple bulk cloud model (e.g., Reed and Johnson, 1974) is adopted for the mesoscale convective motions. Observations from GATE (Houze, 1977; Zipser, 1977; Leary and Houze, 1979b) indicate that these mesoscale systems are characterized by a precipitating mesoscale anvil cloud, presumably containing weak upward motion, based near the melting level (~600 mb) and an unsaturated, evaporatively driven downdraft extending from the vicinity of the melting level to below the level of convective-cloud base. Typical velocities in the downdraft region have been determined to be ~10 cm s^{-1} (Zipser, 1969; Brown, 1979). Leary and Houze (1979b) suggest that the initiation of the downdraft might be a result of cooling caused by the melting of frozen hydrometeors. In the model developed here it is assumed that mesoscale downdrafts occur only for $p \geqslant 600$ mb.

The air motions within and water budgets of precipitating mesoscale anvil clouds in the tropics are still matters of conjecture. Houze *et al.* (1980) present indirect evidence strongly suggesting the presence of upward motion. There remains the possibility, however, that most of the precipitation from mesoscale anvils was originally condensed in cumulonimbus updrafts. In view of these uncertainties we have chosen to ignore mesoscale updrafts. Thus, e_{mu} in (7) and c_{mu} in (8) are zero.

Denoting the mass flux in mesoscale downdrafts by M_{md}, we have

$$M_{md}\frac{\partial h_{md}}{\partial p} = \frac{\partial M_{md}}{\partial p}(\tilde{h} - h_{md}),$$

$$p_B > p \geqslant 600 \text{ mb}, \tag{16}$$

where, as stated earlier, mesoscale downdrafts are assumed to a first approximation to detrain only below the level of updraft cloud base. Each mesoscale system is envisioned here as being associated with one or more cumulonimbus clouds.

There are only a few measurements of the thermo-

TABLE 3. Average mesoscale downdraft thermodynamic structure (from Zipser, 1977).

Pressure level (mb)	Temperature (°C)	Dew point (°C)	Relative humidity (%)	Moist static energy h_{md} (J g^{-1})
600	0.0	−2.2	84	328.4
650	3.8	−0.2	75	327.0
700	8.0	1.5	66	325.7
750	12.0	4.0	59	326.0
800	15.5	6.0	52	325.3
850	19.5	8.0	47	325.6
900	22.0	11.0	48	325.7
950	23.5	13.4	52	325.5

dynamic structure of mesoscale downdrafts. Zipser (1977) summarized a group of soundings taken in mesoscale anvil systems associated with tropical squall lines. Soundings examined in his study are primarily from GATE convective systems although some from the western Atlantic are included. Table 3 presents the temperature, dew point and moist static energy profiles within these systems determined by constructing best-fit curves to seven soundings presented by Zipser. All soundings, as well as some more recent ones obtained in mesoscale anvils off the north coast of Borneo during the Winter MONEX (Winter Monsoon Experiment, December, 1978), exhibit a characteristic "onion-shaped" structure (Zipser, 1977). Within the mesoscale downdrafts below 700 mb h_{md} is approximately constant. This structure is characteristic of these relatively warm, dry downdrafts which possess a relative humidity minimum of 45–50% near 850–900 mb. These soundings are for strong tropical squall-line mesoscale systems and it is likely that the warming and drying in weaker systems is not as extreme.

Profiles of h_{md} and $\bar{h}$ are shown in Fig. 6 for category 2 of the Thompson *et al.* (1979) composite wave. From this figure and (16) we can conclude that M_{md} is approximately constant with height, except in the 600–700 mb layer. In this simple model for the mesoscale downdraft we assume that M_{md} is also approximately constant in the 600–700 mb layer. Zipser's data indicate that $h_{md} \equiv \bar{h}$ near 600 mb, the originating level of the mesoscale downdraft. Accordingly, we assume that mesoscale downdrafts originate at 600 mb with properties of the environmental air. Also shown in Fig. 6 are the cumulus-scale downdraft moist static energy profile h_d for $\lambda = 0.05\ \mathrm{km}^{-1}$, assuming $h_d(\lambda,p_0) = \bar{h}^*(p_0)$ and the saturation moist static energy of the environment $\bar{h}^*$.

Estimates of the fractional area occupied by mesoscale updrafts and downdrafts in tropical disturbances are not available. If they occupy ~10% of the large-scale area, then the representation of fluxes due to mesoscale systems in the same manner as done for cumulus-scale fluxes will be only approximately correct, with neglected terms as large as 10% of those kept (Houze *et al.*, 1980). Nevertheless, we make the approximation that cumulus and mesoscale fluxes can be represented identically:

$$\overline{-\omega' h'} \approx \begin{cases} \displaystyle\int_0^{\lambda_D(p)} m_u(\lambda,p)(h_u - \bar{h})d\lambda + \int_0^{\lambda_D(p)} m_d(\lambda,p)(h_d - \bar{h})d\lambda, & p < 600 \text{ mb} \\ \displaystyle\int_0^{\lambda_D(p)} m_u(\lambda,p)(h_u - \bar{h})d\lambda + \int_0^{\lambda_D(p)} m_d(\lambda,p)(h_d - \bar{h})d\lambda + M_{md}(h_{md} - \bar{h}), & p \geqslant 600 \text{ mb}, \end{cases} \tag{17}$$

where $\lambda_D(p)$, determined from (11) using (9), is the entrainment rate for clouds having their tops at p. Combining (1), (2), (11)–(14), (16), (17) yields

$$Q_1 - Q_2 - Q_R = \begin{cases} \delta(p)[h_u(\lambda_D,p) - \bar{h}(p)] - M_c \dfrac{\partial \bar{h}}{\partial p}, & p < 600 \text{ mb} \\ \delta(p)[h_u(\lambda_D,p) - \bar{h}(p)] - (M_c + M_{md}) \dfrac{\partial \bar{h}}{\partial p}, & \text{for} \quad p_B > p \geqslant 600 \text{ mb}, \end{cases} \tag{18}$$

where

$$M_c = M_u + M_d = \int_0^{\lambda_D(p)} [m_u(\lambda,p) + m_d(\lambda,p)]d\lambda \tag{19}$$

and $\delta(p) \equiv m_u(\lambda_D,p)d\lambda_D/dp$ represents the terminal detrainment rate for clouds with tops at p. Effects of detrainment from the sides of convective-scale updrafts are not necessarily negligible (Johnson, 1977a); however, they will not be included in this study.

The cloud-base mass flux per unit λ in convective-scale updrafts can be expressed in terms of the fractional area occupied by individual updrafts per unit λ, $\sigma_u(\lambda)$, and the vertical velocity at cloud base $\omega_B(\lambda)$:

$$m_B(\lambda) = -\sigma_u(\lambda)\omega_B(\lambda). \tag{20}$$

Similarly, the mass flux in mesoscale downdrafts is

$$M_{md}(p) = -\sigma_m \omega_{md}(p), \tag{21}$$

where σ_m is the fractional area covered by mesoscale downdrafts.

Observational studies cited in the Introduction have shown that mesoscale precipitating systems are the consequence of cumulonimbus convection. The mesoscale anvil develops while the original cumulonimbus convection is still active, and persists for a few hours after most deep convection has ended. The time resolution of the Thompson *et al.* (1979) composite data is insufficient to justify incorporation of this life-cycle effect. In this study each mesoscale system is envisioned as being associated with one more cumulonimbus clouds. It is assumed that the fractional area covered by mesoscale downdrafts is proportional to the fractional area covered by deep cumuli. That is,

$$\sigma_m = c'\sigma_u \text{ (deep clouds)}, \tag{22}$$

where the fractional area occupied by deep cumulonimbus updrafts is

$$\sigma_u \text{ (deep clouds)} = \int_0^{\lambda_D(p')} \sigma_u(\lambda)d\lambda, \tag{23}$$

p' is the pressure delineating the detrainment level of the shortest clouds in the deep-cloud group and c' is a constant. In this study deep clouds are defined as those with tops above 400 mb, i.e., $p' = 400$ mb. This choice would mean that most tropical cumulonimbi are included in the deep-cloud group.

Combining (20)–(23) yields

$$M_{md}(p) = -c'\omega_{md}(p)\int_0^{\lambda_D(p')} \sigma_u(\lambda)d\lambda$$

$$= c'\omega_{md}(p)\int_0^{\lambda_D(p')} \frac{m_B(\lambda)}{\omega_B(\lambda)}d\lambda.$$

Assuming the cloud-base updraft vertical velocity $\omega_B(\lambda)$ to be constant for $0 < \lambda < \lambda_D(p')$ yields

$$M_{md}(p) = c'\frac{\omega_{md}(p)}{\omega_B(\lambda = 0)}\int_0^{\lambda_D(p')} m_B(\lambda)d\lambda. \tag{24}$$

Using (13), (14), (19) and (24) in (18) we obtain

$$Q_1 - Q_2 - Q_R = \delta(p)[h_u(\lambda_D,p) - \bar{h}(p)] - \frac{\partial \bar{h}}{\partial p}\left\{\int_0^{\lambda_D(p)} m_B(\lambda)[\eta_u(\lambda,p) + \epsilon(\lambda)\eta_d(\lambda,p)]d\lambda + \alpha\int_0^{\lambda_D(p')} m_B(\lambda)d\lambda\right\}, \tag{25}$$

where $\epsilon(\lambda)$ is given by (15) and

$$\alpha = \frac{c'\omega_{md}(p)}{\omega_B(\lambda = 0)}.$$

From (22) and the expression above, $\alpha = M_{md}/M_{uD}$ [to the extent that $\omega_B(\lambda)$ is constant for deep clouds] where M_{uD} is the deep-cloud (cloud tops above 400 mb) updraft mass flux at cloud base. Thus, the simple parameterization relating areas of mesoscale systems and cumulonimbus clouds is approximately equivalent to one relating M_{md} to M_{uD} through the constant α. Of course, $\alpha = 0$ for $p < 600$ mb.

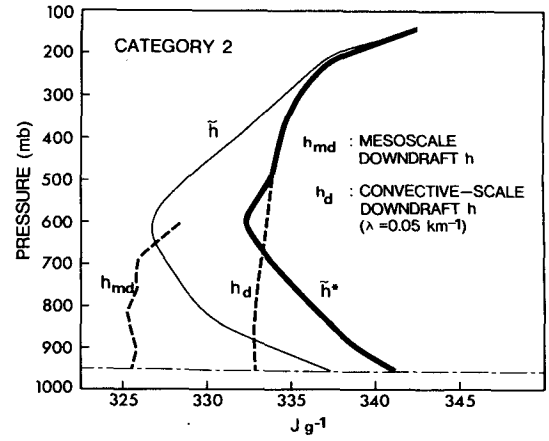

FIG. 6. Mesoscale downdraft moist static energy h_{md}, convective-scale downdraft moist static energy h_d for $\lambda = 0.05$ km^{-1}, environmental moist static energy $\bar{h}$ and saturation moist static energy $\bar{h}^*$.

If α, $\epsilon(\lambda = 0)$ and p_0 can be determined, then (25) can be solved as in Johnson (1976) for the cloud-base-mass-flux-distribution function $m_B(\lambda)$ using large-scale observations. In this study, the solutions of (25) will be determined numerically for plausible values of α with $\epsilon(\lambda = 0)$ and p_0 determined as in Johnson (1976) using a water-vapor budget for the subcloud layer. Properties of the solutions will be examined for a range of mesoscale to convective-scale cloud-area ratios (represented by α).

7. Analysis procedures

Integration of (1) from the tropopause p_T to the surface p_s yields

$$P_0 = g^{-1}\int_{p_T}^{p_s} \frac{Q_2}{L}dp + E_0, \tag{26}$$

where P_0 is the precipitation at the ground and E_0 the surface evaporation. Large-scale observations of q, surface evaporation measurements and computed cloud storage can be used in (26) to determine P_0. Alternatively, we may integrate (1) to cloud base p_B to obtain

$$P_B = g^{-1}\int_{p_T}^{p_B} \frac{Q_2}{L}dp + \frac{M_{uB}}{g}(q_{uB} - \bar{q}_B) + g^{-1}\int_0^{\lambda_D(p_B)} m_d(\lambda,p_B)[q_d(\lambda,p_B) - \bar{q}_B]d\lambda + \frac{M_{mdB}}{g}(q_{mdB} - \bar{q}_B), \tag{27}$$

where P_B is the precipitation at cloud base, subscript B refers to cloud-base values and we have assumed q_{uB} is the same for all cloud types. Eq. (27) can also be used to determine precipitation, but this approach requires a determination of $m_B(\lambda)$. Since $m_B(\lambda)$ depends on Q_1 and Q_R as well as Q_2, (26) and (27), after taking into account precipitation evaporation in the subcloud layer, will not necessarily yield the same P_0. In fact, Johnson (1978) determines $m_B(\lambda)$ [actually $\epsilon(\lambda)$ and $m_B(\lambda)$] by requiring that (26) and (27) give the same precipitation at the ground, where P_0 from (26) agrees well with observed values.

In this study the subcloud water-vapor budget, which depends on surface evaporation E_0, is used to determine $\epsilon(\lambda)$. See Johnson (1976) for discussion of methodology used in this approach. Integration of (1) from the cloud base p_B to the surface p_s yields

$$-g^{-1}\int_{p_B}^{p_s}\frac{Q_2}{L}\,dp = -g^{-1}\overline{(\omega'q')}_s + g^{-1}\overline{(\omega'q')}_B + g^{-1}\int_{p_B}^{p_s}\bar{e}\,dp, \quad (28)$$

where the subscript s refers to surface values and it is assumed that no condensation occurs below cloud base. With $E_0 \equiv -g^{-1}\overline{(\omega'q')}_s$, $\overline{(\omega'q')}_B$ given in form by (17) and using (1) again, Eq. (28) becomes

$$g^{-1}\int_{p_B}^{p_s}\frac{\partial\bar{q}}{\partial t}\,dp + g^{-1}\int_{p_B}^{p_s}\nabla\cdot\bar{\mathbf{v}}\bar{q}\,dp + g^{-1}\bar{M}_B\bar{q}_B = g^{-1}(\bar{e}_d\Delta p + \bar{e}_{md}\Delta p) + E_0 - \frac{M_{uB}}{g}(q_{uB} - \bar{q}_B) - \frac{M_{mdB}}{g}(q_{mdB} - \bar{q}_B) - g^{-1}\int_0^{\lambda_D(p_B)} m_d(\lambda,p_B)[q_d(\lambda,p_B) - \bar{q}_B]\,d\lambda, \quad (29)$$

where $\Delta p = p_s - p_B$ and e_d, e_{md} are subcloud-layer averages.

Terms in (29) from left to right represent the following effects on the water-vapor content of the subcloud layer: water-vapor storage, convergence, mean vertical transport, evaporation associated with convective-scale precipitation, evaporation associated with mesoscale precipitation, surface evaporation, updraft moisture flux, mesoscale downdraft moisture flux and convective-scale downdraft moisture flux, the latter three all evaluated at cloud base. In order to determine $\epsilon(\lambda = 0)$ for each category, Eq. (29) was solved for various $\epsilon(\lambda = 0)$ until a balance was achieved, i.e., the residual was reduced to zero. In some categories the residual approached E_0 in magnitude when convective-scale and mesoscale downdrafts were neglected.

Unlike the western portions of the tropical Atlantic and Pacific, the lower troposphere in the eastern Atlantic is at times only slightly conditionally unstable. The composite wave structure of the saturation moist static energy $\bar{h}^*$ illustrates this situation (Fig. 7). Only slight conditional instability is evident, i.e., $\partial\bar{h}^*/\partial z$ is small in the 900–700 mb layer in categories 1, 6, 7 and 8. As a result $\lambda_D(p)$ is not a single-valued function in these categories as well as in ~50 mb layers in categories 2 and 5. In the shaded region in Fig. 7 $d\lambda_D/dp < 0$, elsewhere it is positive. Clouds reaching their level of zero buoyancy in the shaded layer are those passing from a region of negative buoyancy below to positive buoyancy above and, therefore, no detrainment should be expected in this region. Since detrainment is given by $\delta(p) \equiv m_B(\lambda_D)\eta_u(\lambda_D,p)d\lambda_D/dp$, the thermodynamic data thus require $m_B(\lambda_D) = 0$, where $d\lambda_D/dp < 0$ (δ and $m_B(\lambda_D)$ cannot be negative). Therefore, in this region (25) must take the form

$$Q_1 - Q_2 - Q_R = -\frac{\partial\bar{h}}{\partial p}\left\{\int_0^{\lambda_D(p^*)} m_B(\lambda)[\eta_u(\lambda,p) + \epsilon(\lambda)\eta_d(\lambda,p)]\,d\lambda + \alpha\int_0^{\lambda_D(p')} m_B(\lambda)\,d\lambda\right\}, \quad (30)$$

where p^* is the pressure level of the top of the region. Each category, however, represents a composite of ~20 fitted soundings and obviously on some occasions detrainment must have occurred in this layer. Thus we cannot expect (30) to be satisfied with the observed $Q_1 - Q_2 - Q_R$ in this layer and $m_B(\lambda)$ obtained from (25) for $p < p^*$. To achieve a

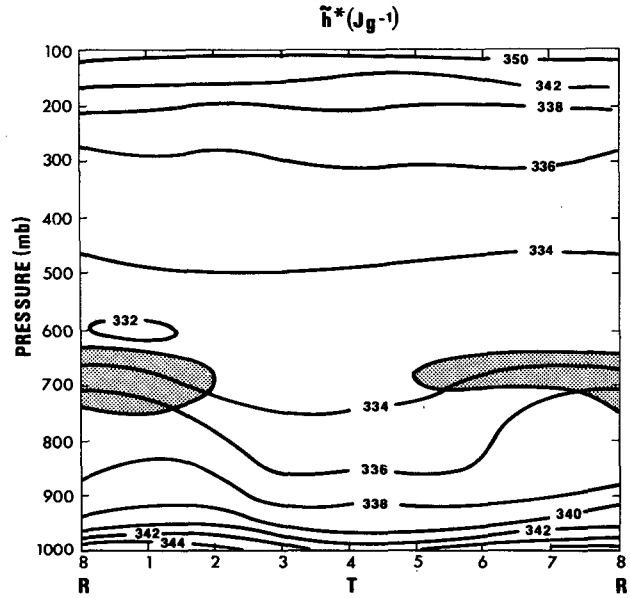

FIG. 7. Saturation moist static energy $\bar{h}^*$ for composite wave. Regions where $d\lambda_D/dp < 0$ are shaded.

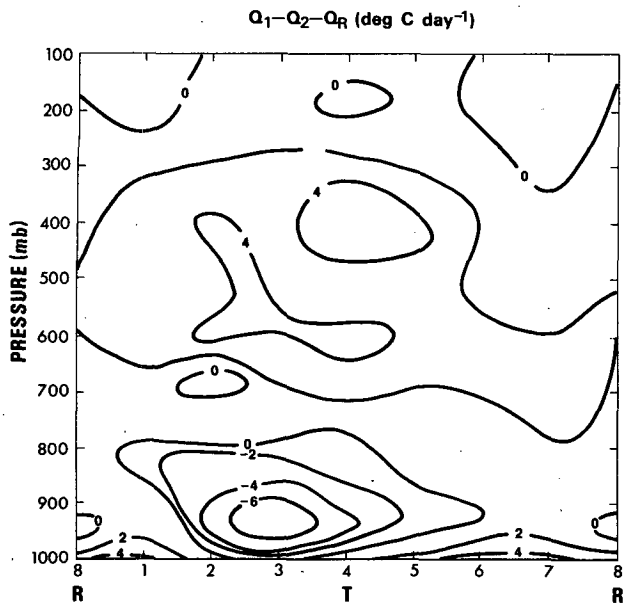

FIG. 8. Moist static energy source $Q_1 - Q_2 - Q_R$.

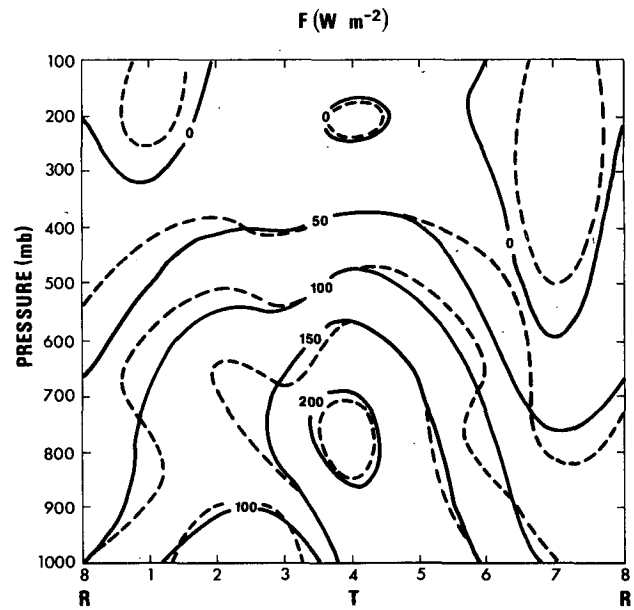

FIG. 9. Vertical eddy heat flux F. Solid lines indicate values computed before correction to $Q_1 - Q_2 - Q_R$ (see text). Dashed lines indicate values after correction has been made.

solution that satisfies (25) for $d\lambda_D/dp > 0$ and (30) for $d\lambda_D/dp < 0$, $Q_1 - Q_2 - Q_R$ has been modified in the ~100 mb layers in categories 1, 6, 7, 8 and ~50 mb layers in 2 and 5 so that (30) is identically satisfied. In order to keep

$$F_0 = g^{-1} \int_{p_T}^{p_s} (Q_1 - Q_2 - Q_R) dp$$

unchanged, a single constant has been added to $Q_1 - Q_2 - Q_R$ at all levels outside this layer. The correction is small. Fig. 8 shows $Q_1 - Q_2 - Q_R$ for the composite wave before the correction is added. A broad maximum of ~4° day^{-1} occurs in the mid-troposphere in the wave trough with a more confined, but stronger minimum (~−6° day^{-1}) centered near cloud base in category 3. The vertical eddy heat flux $F(p)$ computed from these values is shown in Fig. 9 (solid lines). This figure also gives $F(p)$ following application of the correction procedure described above (dashed lines). There is not a significant difference between the two results. Maximum upward transport of total heat is centered above the wave trough with a maximum of ~200 W m^{-2} near 800 mb. A relative minimum, $F < 100$ W m^{-2}, occurs in the lower troposphere in categories 2 and 3. Later results suggest that this feature may be caused by mesoscale downdraft activity in advance of the wave trough. The weak negative values in the upper troposphere may be a reflection of overshooting cumulonimbus towers.

In the following, solutions of (25) for $m_B(\lambda)$ are obtained by specifying the ratio α. Initially, solutions for $\alpha = 0$, -0.5 and -1.0 are examined. The case $\alpha = 0$ corresponds to no mesoscale downdrafts. Estimates that are used for $w_{md} = -\omega_{md}/\rho g$ and $w_B = -\omega_B/\rho g$ are -10 cm s^{-1} and 1 m s^{-1}, respectively. The former estimate is consistent with the findings of Zipser (1977), Brown (1979), Leary and Houze (1979b) and the latter with studies such as Betts *et al.* (1974) and Johnson (1977b). Alternative choices of these values lead to different results for the constant c' in (22) that may be readily determined from the tabulated data to follow.

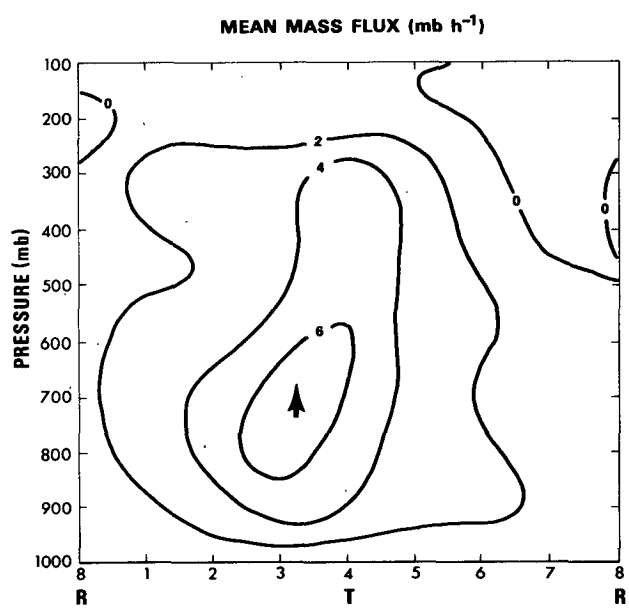

FIG. 10. Mean mass flux $\bar{M}$ for composite wave.

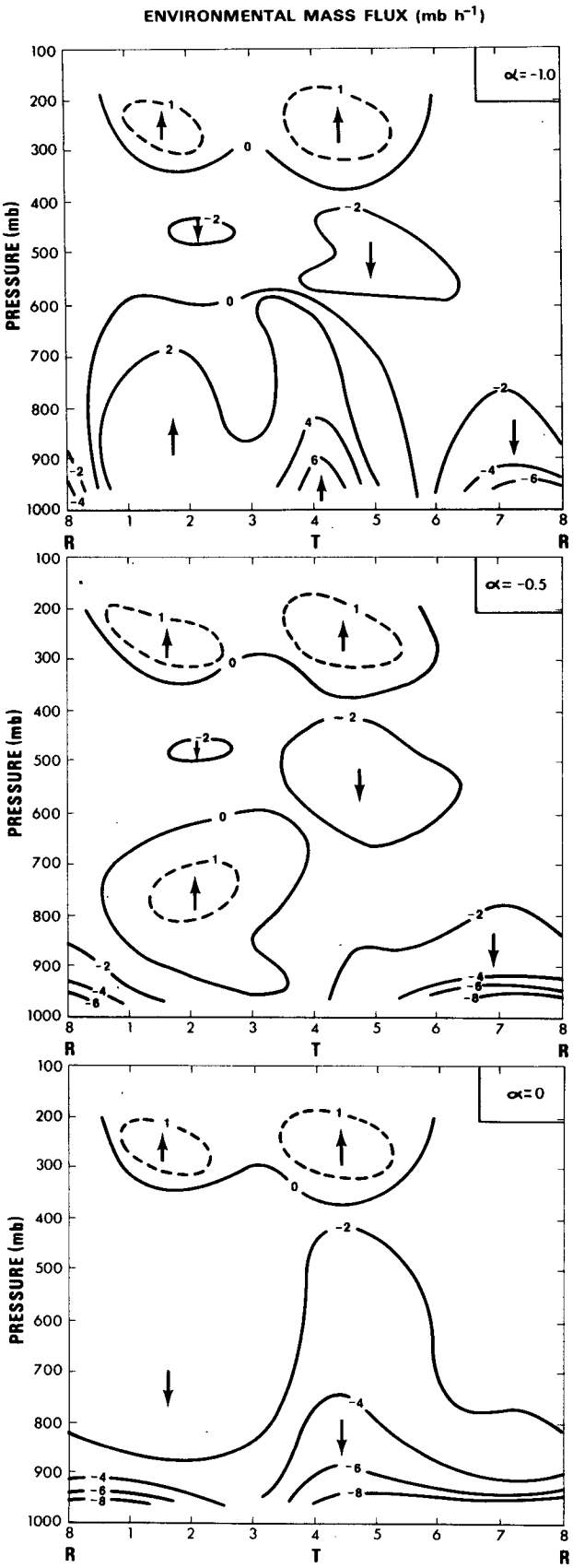

In Table 4, M_{md}, the mesoscale downdraft mass flux, σ_m and σ_u (deep clouds) are given by category for $\alpha = -0.5$ and -1.0. For these particular choices of ω_{md} and ω_B, mesoscale downdrafts occupy an area five times that occupied by deep convective-scale updrafts for $\alpha = -0.5$; and 10 times for $\alpha = -1.0$. For example, in category 4 mesoscale downdrafts occupy 6% of the total area whereas convective-scale downdrafts occupy ~1% for $\alpha = -0.5$. Without highly detailed cloud observations, the predicted area coverages for various α's cannot be verified. However, in general, the results for σ_m and σ_u (deep) are consistent with the assumptions set forth at the outset of this paper.

The convective mass fluxes for $\alpha = 0$, -0.5, -1.0 have been determined for the composite wave. These results can be combined with observations of the mean mass flux $\bar{M} \equiv -\bar{\omega}$ to determine the environmental mass flux $\tilde{M}$ through the relation $\bar{M} = \tilde{M} + M_c + M_{md}$. The mean mass flux is shown in Fig. 10. Maximum upward motion of ~6 mb h^{-1} occurs near 700 mb between categories 3 and 4. A weak secondary maximum exists near 350 mb in categories 1–5.

The solutions for $\tilde{M}$ for the three choices of α are shown in Fig. 11. These results will form the basis for the selection of an α that gives the most realistic mesoscale-downdraft mass-flux estimates. For $\alpha = 0$, very strong subsidence is seen to exist in the lower troposphere in nearly all portions of the wave. However, since extensive low cloudiness (~50% or more) was observed in categories 2–4 (Table 1), strong subsidence in the active-cloud environment, i.e., the regions between convective and mesoscale draft systems, must be ruled out. Therefore, the case $\alpha = 0$ is not realistic. On the other hand, for $\alpha = -1.0$ lower tropospheric subsidence occurs only in the wave ridge with rather substantial upward motion throughout the lower troposphere from categories 1 to 5. This situation is also not reasonable since this result would suggest virtually complete cloud cover in the active cloud environment through the entire troposphere in these categories. By contrast, $\tilde{M}$ for $\alpha = -0.5$ exhibits features that one might expect in the cloudy region in advance of the wave trough: weak subsidence near cloud base with only slight upward motion above extending to 600 mb. Although the above arguments do not yield a precise quantitative determination of α, it is concluded that $\alpha = -0.5$ is the most reasonable choice of the three above. Further refinement of this aspect of the model requires more comprehensive measurements of cloud cover and convective-scale and mesoscale downdraft areas than are presently

FIG. 11. Environmental mass flux $\tilde{M}$ for composite wave for $\alpha = 0, -0.5, -1.0$.

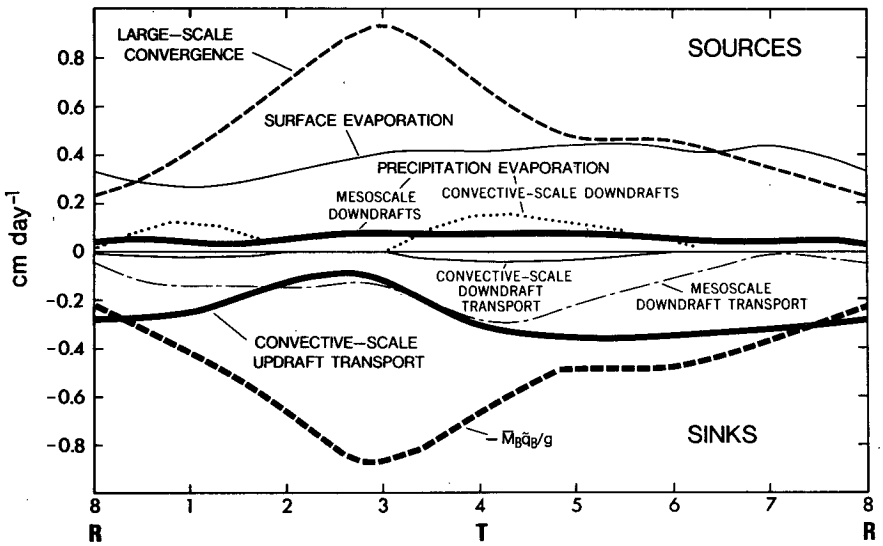

FIG. 12. Subcloud-layer water-vapor budget for composite wave.

available. We will henceforth confine discussion to results for $\alpha = -0.5$.

8. Results for $\alpha = M_{md}/M_{uD} = -0.5$

Terms in the subcloud layer water vapor budget are shown in Fig. 12. In categories 1–4 the primary moisture source, large-scale convergence, exceeds evaporation from the ocean surface. Large-scale convergence in the subcloud layer is sufficient to account for only ~40% of the observed precipitation minus evaporation in this portion of the wave (Table 2), suggesting that a substantial portion of the moisture convergence into clouds is above cloud base. The decomposition of the flow into a mean plus deviation leads to the term $\bar{M}_B\bar{q}_B/g$ in (29) that represents the transport of water vapor out of the subcloud layer by the mean vertical motion. In reality, water vapor is transported upward in cumulus updrafts and downward in downdrafts and by environmental subsidence, processes that can be represented by transforming (29) into an alternative form that expresses these transports (e.g., Ogura and Cho, 1974; Johnson, 1976). However, in order to interpret the updraft and downdraft transports in terms of fluxes, Eq. (29) is kept in its original form. The transport of water vapor by the mean circulation $\bar{M}_B$ is shown as the major sink of water vapor for the subcloud layer. Convective-scale updrafts and downdrafts and mesoscale downdrafts also act to reduce the specific humidity of the subcloud layer. In the wave trough region the relatively dry mesoscale downdrafts are as important a water vapor sink as convective-scale updraft transport. The net effect of convective-scale downdraft transport on the water-vapor content of the subcloud layer is small.

Precipitation evaporation moistens the subcloud layer with both convective-scale and mesoscale downdrafts contributing equally. Evaporation in convective-scale downdrafts is determined by assuming that the subcloud layer evaporation rate is equivalent to that at cloud base given by the cloud-layer model. Mesoscale precipitation evaporation is estimated from the evaporation expression derived by Ogura and Takahashi (1971) using Zipser's (1977) downdraft sounding data and the composite wave precipitation data. For the purposes of this calculation it is assumed that 40% of the total precipitation is mesoscale (Cheng and Houze, 1980). Since the downdraft evaporation terms are small in (29), overall results are not particularly sensitive to this assumption. Precipitation evaporation is generally considerably less than evaporation from the ocean surface. The storage term in (29) is nearly zero in all categories.

These results suggest that mesoscale downdrafts contribute significantly to the water-vapor budget for the subcloud region of African wave disturbances in the GATE area. Their effects on the budget in disturbed conditions are comparable to those of cumulus-scale updrafts. It is apparent that theories for the parameterization of moist convection in large-scale numerical prediction models must in some way include the effects of mesoscale as well as convective-scale downdrafts if accurate predictions of boundary-layer moisture are required. Similar conclusions have been reached by Miller and Betts (1977) in a study of tropical squall systems over Venezuela.

The cumulus updraft mass flux M_u and downdraft mass flux M_d are shown in Fig. 13a. Maximum updraft mass flux occurs at the wave trough with

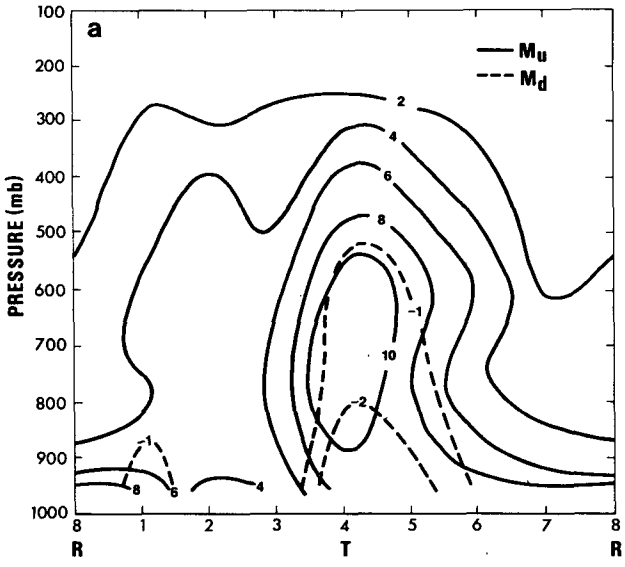

FIG. 13a. Updraft and downdraft mass fluxes M_u and M_d for composite wave.

an amplitude of ~11 mb h^{-1} near 700 mb. A weaker secondary maximum in the mid-troposphere occurs near category 2, well ahead of the trough. The position of the latter feature coincides with the preferred location for squall development in the African waves as reported by Payne and McGarry (1977). The major squall systems studied by Houze (1977) and Zipser (1977) all occurred in categories 1, 2 or 3 of their associated waves. The presence of these convective systems in advance of the trough is clearly evident in Fig. 13a. Cumulus downdrafts are strongest in category 4 with a mass-flux amplitude at cloud base about 30% that of updrafts. A weaker maximum occurs at cloud base in category 1. The mesoscale downdraft mass flux M_{md} is illustrated in Fig. 13b. Weak mesoscale downdrafts occur from categories 1–5 with a peak slightly $\geqslant -2$ mb h^{-1} in category 4.

As determined in earlier GATE studies (Nitta, 1977; Johnson, 1978) a bimodal distribution of clouds, both deep and shallow, are prevalent in the GATE region. However, it was noted that shallow cumulus activity was a minimum when deep convection was a maximum, and conversely. The detrainment rate shown in Fig. 14 for the cloud population in the composited wave also indicates this same result. A minimum of shallow cumuli exists in categories 2–4 with a maximum centered about the ridge. Maximum detrainment in the upper troposphere occurs near 300 mb in categories 2–5.

Figs. 13 and 14 lead to the following interpretation of convective activity associated with the composite African wave. After passage of the ridge deep convection develops in category 1. Mesoscale downdrafts also are first observed in this category. Cumulus-scale downdrafts then diminish in categories 2 and 3 while mesoscale downdrafts continue. The solution for $\tilde{M}$ in Fig. 11 shows rising motion to exist at 200–300 mb in this region of the wave (as well as in the trough). This feature may be associated with widespread upward motion present in the upper portion of mesoscale anvils. Cumulus-scale updrafts and downdrafts and mesoscale downdrafts then increase to a maximum in the wave trough. A peak in detrainment is also found in the wave trough in the mid-troposphere near 500 mb. These findings are consistent with the results of Thompson *et al.* (1979) which suggest three primary levels of detrainment corresponding well to those found in this study.

A small region of negative δ is seen in categories 2 and 3 near cloud base. As noted earlier (Fig. 3) the apparent moisture sink Q_2 is large in this region. From the following form of the water-vapor equation for the cloud models used here

$$-\frac{Q_2}{L} = -(M_c + M_{md})\frac{\partial \tilde{q}}{\partial p} + \tilde{e}_u + \delta[q_u(\lambda_D,p) - \tilde{q}], \quad (31)$$

it is seen that the only drying mechanism that can account for the large Q_2 is environmental sinking compensating the net convective-mass flux $M_c + M_{md}$. Evaporation of detrained liquid water and detrainment of water vapor from updrafts are both moistening processes. Since for $\alpha = -0.5$ environmental subsidence in this region is small, negative values of δ are necessary to achieve a solution to (31) near cloud base in categories 2 and 3. This result points to a deficiency in the cloud models

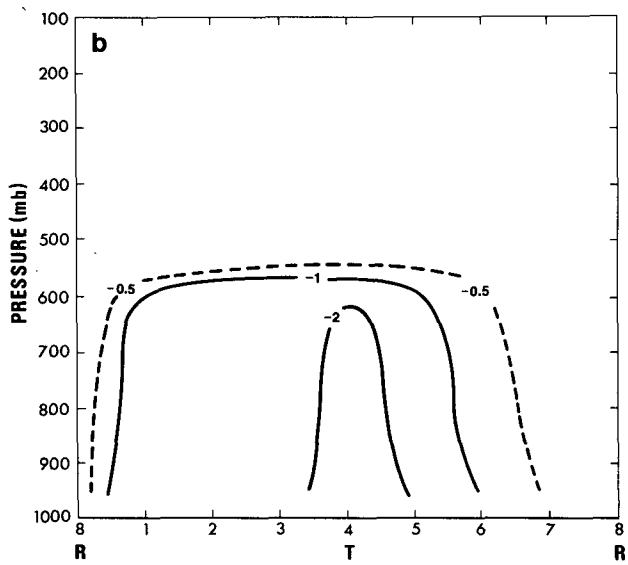

FIG. 13b. Mesoscale downdraft mass flux M_{md}. Units: mb h^{-1}.

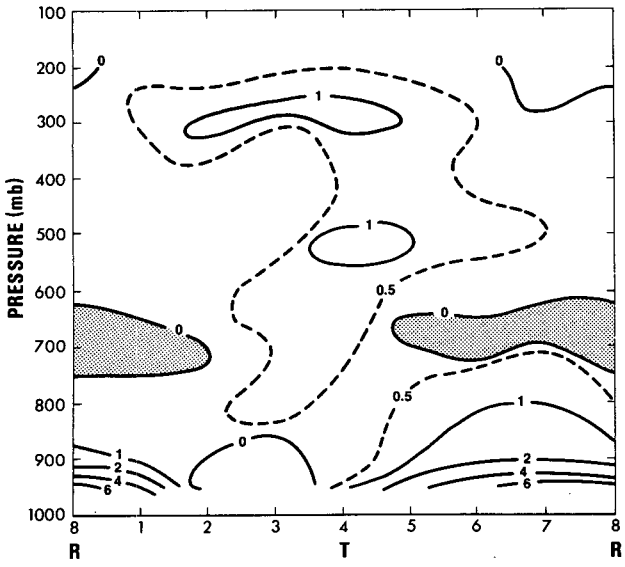

FIG. 14. Detrainment rate (day^{-1}) from cumulus updrafts. In shaded region $d\lambda_D/dp < 0$, i.e., no detrainment is permitted.

used in this study. It is apparent that some process not represented in (31) operates to dry the air just above cloud base in advance of the trough. A possible process to account for this effect is detrainment from mesoscale downdrafts above cloud base. Had mesoscale downdraft detrainment been included in the model, Eq. (31) would have been primarily a balance between the large moisture sink Q_2 in this region and detrainment of lower specific humidity air from mesoscale downdrafts.

The work of Johnson (1978) showed that deep convection in African waves is related to large-scale, low-level convergence although the relationship apparently varies with latitude. This study for the B-scale array indicates that maximum deep-cloud mass flux M_{uD} (mass flux at cloud base due to updrafts with tops above 400 mb) occurs ~12 h after a maximum in the mean mass flux at 950 mb $\bar{M}_{950}$ (Fig. 15). A much smaller phase lag was determined between M_{uD} and $\bar{M}_{950}$ at this latitude in Johnson (1978). It is felt that the results reported here present a more reliable picture of the true phase relationships since the earlier study used a combination of land and ocean data. The delay in the response in deep-cloud activity to large-scale, low-level convergence was attributed to Johnson (1978) to gradual moistening effects of a deepening layer of shallow cumulus clouds in advance of the wave trough. The relative humidity profile for the wave (Thompson *et al.*, 1979) indicates significant moistening in the lower troposphere in this region. However, the absence of shallow cumuli in categories 2 and 3 (Fig. 14) suggests that in this case another explanation is needed. The observed moistening may be a result of the large increase in inactive low-cloud amount ahead of the trough (Table 1), or precipitation evaporation in mesoscale downdrafts or a combination of both. The way in which these features might contribute to a 12 h delay in the response of deep convection to low-level forcing, beyond simply providing a more moist environment for deep cumulus growth is not clear, however. The deep cloud mass flux M_{uD} correlates well with high or bright convective cloud amount as reported by Thompson *et al.* (1979). The secondary peaks in M_{uD} and high cloud amount near category 2 are consistent with the existence of squall-type convection ahead of the wave trough as discussed earlier. Since the parameterization

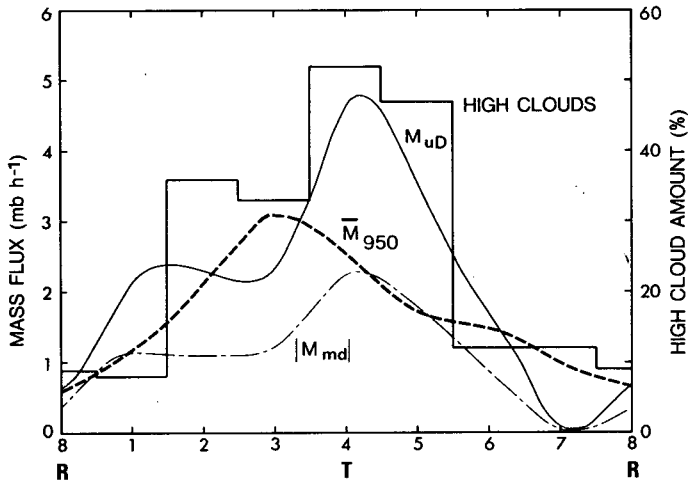

FIG. 15. Deep cumulus mass flux M_{uD}, large-scale mass flux at 950 mb $\bar{M}_{950}$, absolute value of mesoscale downdraft mass flux $|M_{md}|$, and high cloud amount for composite wave (latter from Thompson *et al.* 1979).

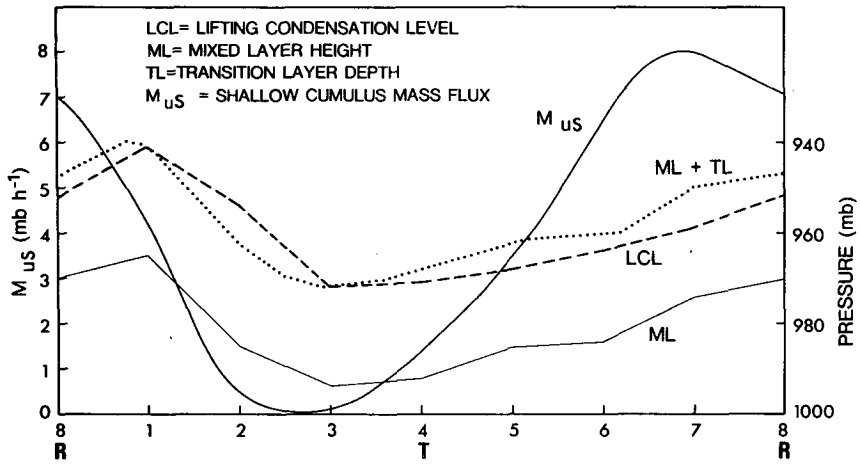

FIG. 16. Shallow cumulus mass flux M_{uS}, lifting condensation level of surface air LCL, mixed-layer height ML, and ML plus transition layer depth TL for composite wave. ML and LCL are for 15–18 September wave (from Payne, 1978).

used in this study ties mesoscale downdraft activity to deep-cumulus updraft activity, $|M_{mD}|$ and M_{uD} in Fig. 15 have similar shapes.

As previously mentioned, a minimum in shallow cumulus activity occurs in categories 2–4. Johnson (1978) suggested that a major cause of this feature is stabilization of the subcloud layer by convective-scale downdrafts. The significant variation of shallow cumulus activity with wave phase is evident in Fig. 16. In this figure M_{uS} is the cloud-base mass flux due to clouds with tops below 750 mb. M_{uS} exhibits a nearly sinusoidal variation with minimum and maximum amplitudes in categories 3 and 7. To investigate further the cause of this variation, mixed-layer depth data for an individual wave from Payne (1978) are also plotted in Fig. 16. Payne determined average mixed-layer heights from rawinsonde observations during the passage of an African wave during the period 15–18 September. It is assumed that this variation is typical of all waves during Phase III. The mixed layer is observed to be deepest in the wave ridge and shallowest at and just in advance of the wave trough. The shallowing of the mixed layer in the wave trough suggests the possibility that shallow cumuli diminish in this region because eddies within the mixed layer can no

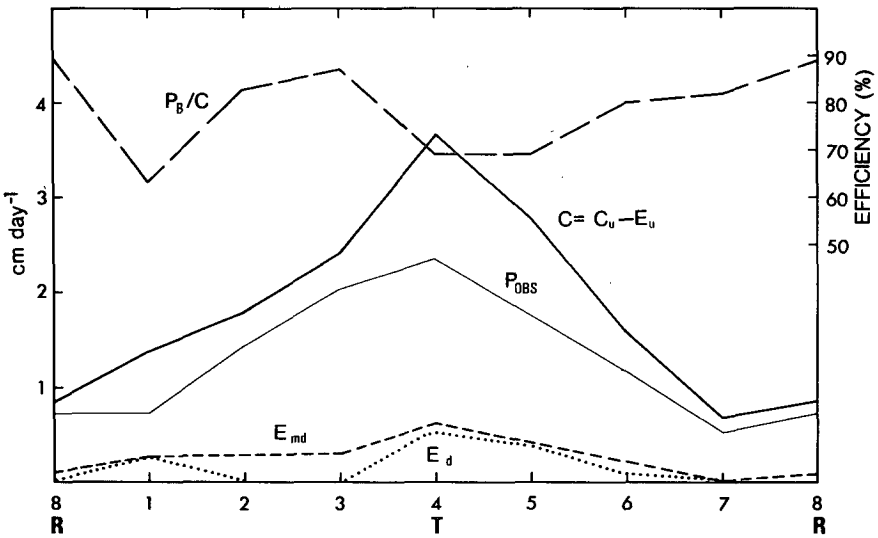

FIG. 17. Total water budget for composite wave. C_u is updraft condensation, E_u evaporation of detrained liquid water from updrafts, E_{md} evaporation in mesoscale downdrafts, E_d evaporation in convective-scale downdrafts, P_B precipitation at cloud base and P_{OBS} observed precipitation. Cloud efficiency is defined as P_B/C, where $C = C_u - E_u$.

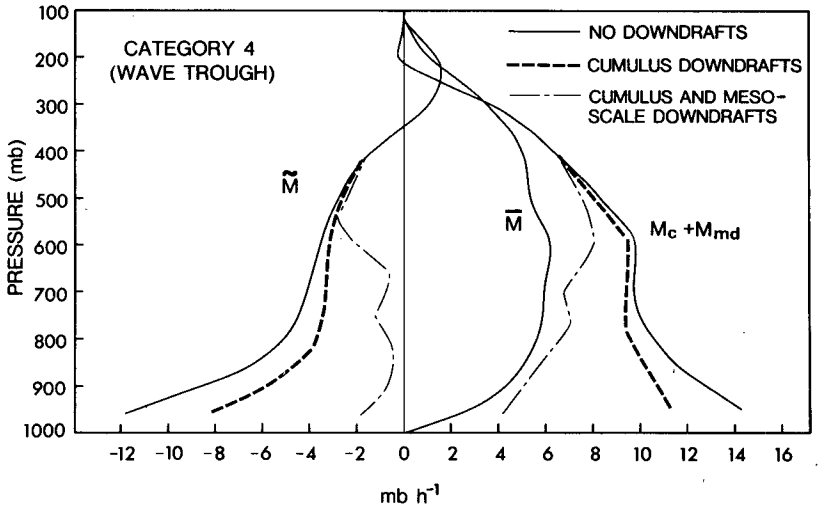

FIG. 18. Environmental mass flux $\tilde{M}$, mean mass flux $\bar{M}$ and net convective mass flux $M_c + M_{md}$ for category 4 for cases with and without downdrafts.

longer extend to the lifting condensation level of the surface air, even allowing for some overshooting. If the Phase III averaged observed transition-layer depth (~25 mb) for both undisturbed and disturbed situations (C. F. Ropelewski, personal communication, NOAA/CEAS, Washington, DC) is added to the mixed layer depth, the dotted curve in Fig. 16 is obtained. Comparing this curve with the composite lifting condensation level (LCL), we see that from categories 1–3 the top of the transition layer is below the LCL of the surface air. Such a situation would lead to a suppression of shallow cumuli, as is observed. On the other hand, the top of the transition layer is above the LCL in categories 4–8. This situation is favorable for the development of shallow cumuli, and is consistent with the observed maximum in M_{uS} in these categories. There are admittedly a number of uncertainties in the above analysis and it is likely that a study of processes that control shallow cloud populations can best be done with a case-study approach.

The total water budget for the composite wave is shown in Fig. 17. Since total evaporation of detrained water from updrafts E_u was computed to be small and sometimes negative, this term is combined with the total condensation in updrafts C_u to give $C = C_u - E_u$ or the rate at which condensate is supplied by updrafts for precipitation and evaporation in downdrafts. In the wave trough (category 4) ~30% of the condensed water is evaporated in convective-scale and mesoscale downdrafts (equally divided between both). In advance of the trough most precipitation evaporation is in mesoscale downdrafts. Cloud efficiency, defined as the ratio of total precipitation at cloud base P_B to C averages 78% for the composite wave.

9. Comparison with no-downdraft cases

The previous studies of Johnson (1976) and Nitta (1977) have demonstrated that convective-scale downdrafts are important contributors to the total convective mass flux in tropical disturbances. It was suggested that prognostic models that use cloud models for parameterization for moist convection would overestimate subsidence between clouds and, hence, predict excessive warming in the lower troposphere if cumulus downdrafts were ignored. The study of Johnson (1976) using western Pacific data indicated that the diagnosed environmental subsidence in disturbed conditions is reduced by approximately one-half when convective-scale downdrafts are taken into account. Even further reductions are realized when mesoscale downdrafts are included (Fig. 11). These effects are summarized in Fig. 18 for the wave trough. When no downdrafts are included in the diagnostic model, the net cumulus and mesoscale mass flux $M_c + M_{md}$ at cloud base is large, ~14 mb h^{-1}. Since the mean mass flux $\bar{M}$ at cloud base is comparatively small, $|\tilde{M}|$ is also large at this level. When convective-scale downdrafts are included, both $M_c + M_{md}$ and $|\tilde{M}|$ are reduced by ~25% at cloud base. However, a considerably larger reduction occurs in $M_c + M_{md}$ and $|\tilde{M}|$ when mesoscale downdrafts are also included.

10. Summary and conclusions

Observations of tropical-wave disturbances during GATE have shown that a variety of convective-system types contributed to rainfall over the ship array. Two types of downdrafts, convective-scale and mesoscale, were prominent features of many

TABLE 4. Mesoscale downdraft mass flux M_{md} (mb h^{-1}), fractional areas occupied by mesoscale downdrafts σ_m and cumulonimbus updrafts σ_u (deep) as a function of α. $c' = \sigma_m/\sigma_u$ (deep) is computed assuming $w_{md}(p_B) = -\omega_{md}/\rho g = -10$ cm s^{-1} and $w_B = -\omega_B/\rho g = 1$ m s^{-1}.

		Category							
		1	2	3	4	5	6	7	8
$\alpha = -0.5$	M_{md}	−1.10	−1.14	−1.15	−2.31	−1.71	−0.81	0.00	−0.36
$c' = 5$									
	σ_m	0.03	0.03	0.04	0.06	0.05	0.02	0.00	0.01
	σ_u (deep)	0.006	0.006	0.008	0.012	0.010	0.004	0.00	0.002
$\alpha = -1.0$	M_{md}	−2.20	−2.28	−2.30	−4.62	−3.42	−1.62	0.00	−0.72
$c' = 10$	σ_m	0.06	0.06	0.08	0.12	0.10	0.04	0.00	0.02
	σ_u (deep)	0.006	0.006	0.008	0.012	0.010	0.004	0.00	0.002

of the disturbances. A diagnostic model has been developed to determine the properties of cumulus populations, taking into account effects of cumulus-scale and mesoscale updrafts and downdrafts. As in the previous study by Johnson (1976) an entraining-plume model is used for cumulus updrafts and downdrafts. In this study the parameter $\epsilon(\lambda)$, the ratio of the cumulus-downdraft mass flux at the originating level of the downdraft to the updraft mass flux at cloud base, is given as a function of cloud size. Its functional form is such that downdrafts from shallow clouds are practically negligible. Mesoscale downdrafts are modeled using a bulk or single-mass-flux model. In the application of the model to GATE data it is assumed that all precipitation that occurs in mesoscale downdrafts is originally generated in cumulus updrafts. This assumption implies that mesoscale updraft motion is neglected. The solution of the problem then depends on the modeling of the mesoscale downdraft.

Observations within mesoscale downdrafts taken from Zipser (1977) are used to specify their temperature and moisture distributions. These downdrafts are assumed to start near the melting level at 600 mb. A parameterization is introduced to relate the fractional area occupied by mesoscale downdrafts to the fractional area occupied by cumulonimbus convection. Determination of a best estimate of mesoscale downdraft intensities is based on a physical interpretation of the diagnosed environmental subsidence in light of observed cloud cover for the wave. This method suggests $\alpha = M_{md}/M_{uD} \approx -0.5$, i.e., the mass flux in mesoscale downdrafts (M_{md}) is one-half that at cloud base due to updrafts that detrain above 400 mb (M_{uD}).

The model is applied to composite-wave data from the B-scale ship array of GATE (Thompson *et al.*, 1979). An evaluation of cloud-water storage effects based on GATE whole-sky camera cloudiness data shows that cloud storage is of some importance in the water budget in regions of the wave where cloud cover is rapidly changing. Radiative heating rates from Cox and Griffith (1979) for Phase III of GATE are used in the computations of convective transports in the wave. Results suggest that mesoscale downdraft mass fluxes in the lower troposphere are comparable in magnitude to convective-scale fluxes. Mesoscale downdrafts are found to contribute importantly to the subcloud-layer water-vapor budget by transporting relatively dry air into the subcloud layer. The net upward cumulus mass flux during convectively disturbed conditions is reduced considerably when the effects of mesoscale downdrafts are included in the diagnostic model. Consequently, the magnitude of the diagnosed environmental subsidence is also reduced. This finding has important implications for prognostic models of the Arakawa-Schubert type since environmental subsidence is an important heating and drying mechanism on the large scale. It is evident, at least in the tropical eastern Atlantic, that the effects of mesoscale downdrafts in

TABLE 5. Mesoscale downdraft and total precipitation rates. Units: mm day^{-1}.

	Category								
Rain type	1	2	3	4	5	6	7	8	Mean
Mesoscale	3.6	3.6	4.8	7.2	6.0	2.4	0.0	1.2	3.6
Mesoscale and convective scale	3.6	16.2	19.5	22.0	21.1	5.9	7.9	4.0	12.5

cumulus parameterization theories must be included if accurate predictions of both water vapor in the subcloud layer and lower tropospheric temperature and moisture fields are required. Although these results provide a qualitative estimate of mesoscale downdraft effects, it is clear that the method of determining mesoscale downdraft intensities is not fully satisfactory. Further improvements in modeling these mesoscale systems as well as improved cloud observations appear to be necessary for a precise determination of the contributions of each convective phenomena to the total convective transport.

An obvious shortcoming of the proposed model is the neglect of mesoscale updrafts. With this assumption, we require all rain to be generated within cumulus updrafts. An estimate of the amount of rainfall implied by the mesoscale model can be made from observational data and model results. Leary and Houze (1979b) note that the GATE mesoscale downdraft systems they studied having a downdraft velocity ~ -10 cm s^{-1} were characterized by precipitation rates 1–10 mm h^{-1}. Using the values of σ_m in Table 4 for $\alpha = -0.5$ and assuming an average rainfall rate in mesoscale downdrafts of 5 mm h^{-1} based on Leary and Houze (probably an upper bound for Phase III as a whole), mesoscale precipitation rates have been determined and are shown in Table 5. It is seen that on the average for the composite wave under the assumptions of this study $\sim$30% of the total precipitation occurs in mesoscale downdrafts. Comparing with Fig. 17, we see that the mesoscale precipitation reaching the ground is roughly equal to the amount of evaporation in mesoscale downdrafts. Using radar data, Cheng and Houze (1979) found that about 40% of the total precipitation in GATE was from mesoscale convection.

Clearly, further improvements in the modeling of mesoscale updrafts and downdrafts should provide improved estimates of their contribution to the total convective transports in tropical disturbances. Nevertheless, it is felt that this study has demonstrated the probable importance of these systems and has provided a semi-quantitative determination of the effects of mesoscale downdrafts on the subcloud layer water vapor budget and diagnosed environmental subsidence in the lower troposphere. Detailed verification of the model predictions is difficult since GATE measurements, as good as they are, do not allow precise determination of fractional area coverages of cumulus-scale and mesoscale convective systems over the entire B-array.

Acknowledgments. My appreciation is extended to John M. Brown, NCAR, for a highly constructive review of this paper. Thanks go to Richard J. Reed and his research group at the University of Washington for supplying the tropical wave composite data. I also thank David Priegnitz and Mark Wysocki for their assistance with data reduction. The research has been supported by the National Science Foundation and National Oceanic and Atmospheric Administration under Grant ATM78-11633 and the University of Wisconsin-Milwaukee Graduate School.

REFERENCES

Arakawa, A., and W. Schubert, 1974: Interaction of cumulus cloud ensemble with the large-scale environment, Part I. *J. Atmos. Sci.*, **31**, 674–701.

Betts, A. K., F. J. Dugan and R. W. Grover, 1974: Residual errors of the VIZ radiosonde hygrister as deduced from observations of the subcloud layer structures. *Bull. Amer. Meteor. Soc.*, **55**, 1123–1125.

Brown, J. M., 1979: Mesoscale unsaturated downdrafts driven by rainfall evaporation: A numerical study. *J. Atmos. Sci.*, **36**, 313–338.

Brümmer, B., 1978: Mass and energy budgets of a 1 km high atmospheric box over the GATE C-scale triangle during undisturbed and disturbed weather conditions. *J. Atmos. Sci.*, **35**, 997–1011.

Cheng, C. -P., and R. A. Houze, Jr., 1979: The distribution of convective and mesoscale precipitation in GATE radar echo patterns. *Mon. Wea. Rev.*, **107**, 1370–1381.

——, and ——, 1980: Sensitivity of diagnosed convective fluxes to model assumptions. *J. Atmos. Sci.*, **37**, 774–783.

Cox, S. K., and K. T. Griffith, 1979: Estimates of radiative divergence during Phase III of the GARP Atlantic Tropical Experiment: Part II. Analysis of Phase III results. *J. Atmos. Sci.*, **36**, 586–601.

Dopplick, T. G., 1972: Radiative heating of the global atmosphere *J. Atmos. Sci.*, **29**, 1278–1294.

Holle, R. L., J. Simpson and S. W. Leavitt, 1979: GATE B-scale cloudiness from whole-sky cameras on four U.S. ships. *Mon. Wea. Rev.*, **107**, 874–895.

Houze, R. A., 1977: Structure and dynamics of a tropical squall-line system observed during GATE. *Mon. Wea. Rev.*, **105**, 1540–1567.

——, C. -P. Cheng, C. A. Leary and J. F. Gamache, 1980: Diagnosis of cloud mass and heat fluxes from radar and synoptic data. *J. Atmos. Sci.*, **37**, 754–773.

Johnson, R. H., 1976: The role of convective-scale precipitation downdrafts in cumulus and synoptic-scale interactions. *J. Atmos. Sci.*, **33**, 1890–1910.

——, 1977a: The effects of cloud detrainment on the diagnosed properties of cumulus populations. *J. Atmos. Sci.*, **34**, 359–366.

——, 1977b: Effects of cumulus convection on the structure and growth of the mixed layer over south Florida. *Mon. Wea. Rev.*, **105**, 713–724.

——, 1978: Cumulus transports in a tropical wave composite for Phase III of GATE. *J. Atmos. Sci.*, **35**, 484–494.

Leary, C. A., and R. A. Houze, 1979a: The structure and evolution of convection in a tropical cloud cluster. *J. Atmos. Sci.*, **36**, 437–457.

——, and ——, 1979b: Melting and evaporation of hydrometeors in precipitation from the anvil clouds of deep tropical convection. *J. Atmos. Sci.*, **36**, 669–679.

——, and ——, 1980: The contribution of mesoscale motions to the mass and heat fluxes of an intense tropical convective system. *J. Atmos. Sci.*, **37**, 784–796.

Lopez, R. E., 1978: Internal structure and development processes of C-scale aggregates of cumulus clouds. *Mon. Wea. Rev.*, **106**, 1488–1494.

McGarry, M. M., and R. J. Reed, 1978: Diurnal variations in convective activity and precipitation during Phases II and III of GATE. *Mon. Wea. Rev.*, **106**, 101–113.

McNab, A. L., and A. K. Betts, 1978: A mesoscale budget study of cumulus convection. *Mon. Wea. Rev.*, **106**, 1317–1331.

Miller, M., and A. K. Betts, 1977: Traveling convective storms over Venezuela. *Mon. Wea. Rev.*, **105**, 833–848.

Nitta, T., 1975: Observational determination of cloud mass flux distributions. *J. Atmos. Sci.*, **32**, 73–91.

——, 1977: Response of cumulus updraft and downdraft to GATE A/B-scale motion systems. *J. Atmos. Sci.*, **34**, 1163–1186.

Ogura, Y., and T. Takahashi, 1971: Numerical simulation of the life cycle of a thunderstorm cell. *Mon. Wea. Rev.*, **99**, 895–911.

——, and H. R. Cho, 1973: Diagnostic determination of cumulus cloud populations from observed large-scale variables. *J. Atmos. Sci.*, **30**, 1276–1286.

——, and ——, 1974: On the interaction between the subcloud and cloud layers in tropical regions. *J. Atmos. Sci.*, **31**, 1850–1859.

Payne, S., 1978: The large scale structure and properties of the disturbance of 15 to 18 September, 1974, over the GATE B-scale ship array. M.S. thesis, University of Washington, 112 pp.

——, and M. M. McGarry, 1977: The relationship of satellite inferred convective activity to easterly waves over West Africa and the adjacent ocean during Phase III of GATE. *Mon. Wea. Rev.*, **105**, 413–420.

Reed, R. J., and R. H. Johnson, 1974: The vorticity budget of synoptic-scale wave disturbances in the tropical western Pacific. *J. Atmos. Sci.*, **31**, 1784–1790.

——, D. C. Norquist and E. E. Recker, 1977: The structure and properties of African wave disturbances as observed during Phase III of GATE. *Mon. Wea. Rev.*, **105**, 317–333.

Thompson, R. M., S. W. Payne, E. E. Recker and R. J. Reed, 1979: Structure and properties of synoptic-scale wave disturbances in the intertropical convergence zone of the eastern Atlantic. *J. Atmos. Sci.*, **36**, 53–72.

Yanai, M., S. Esbensen and J. H. Cho, 1973: Determination of bulk properties of tropical cloud clusters from large-scale heat and moisture budgets. *J. Atmos. Sci.*, **30**, 611–627.

——, J. H. Cho, T. E. Stark and T. Nitta, 1976: Response of deep and shallow tropical maritime cumuli to large-scale processes. *J. Atmos. Sci.*, **33**, 976–991.

Zipser, E. J., 1969: The role of organized unsaturated convective downdrafts in the structure and rapid decay of an equatorial disturbance. *J. Appl. Meteor.*, **8**, 799–814.

——, 1977: Mesoscale and convective-scale downdrafts as distinct components of squall-line circulation. *Mon. Wea. Rev.*, **105**, 1568–1589.